




NOTE

4D flow imaging with UNFOLD in a reduced FOV

Clarissa Wink^{1,2}  | Jean Pierre Bassenge^{1,3} | Giulio Ferrazzi^{1,4} | Tobias Schaeffter^{1,2}  | Sebastian Schmitter¹ 

¹Physikalisch-Technische Bundesanstalt (PTB), Braunschweig and Berlin, Germany

²FG Medizintechnik, Technische Universität Berlin, Berlin, Germany

³Working Group on Cardiovascular Magnetic Resonance, Experimental and Clinical Research Center, a joint cooperation between the Charité Medical Faculty and the Max-Delbrueck Center for Molecular Medicine, Berlin, Germany

⁴Division of Imaging Sciences and Biomedical Engineering, King's College London, London, United Kingdom

Correspondence

Clarissa Wink, Department of Biomedical Magnetic Resonance, Physikalisch-Technische Bundesanstalt, Abbestr. 2-12, 10587 Berlin, Germany.
Email: Clarissa.Wink@ptb.de

Funding information

Deutsche Forschungsgemeinschaft, Grant/Award Number: GRK2260 and BIOQIC; German Research Foundation (DFG), Grant/Award Number: SCHM 2677/2-1

Purpose: Two-dimensional selective excitation (2DRF) allows shortening 4D flow scan times by reducing the FOV, but the longer 2DRF pulse duration decreases the temporal resolution, yielding underestimated peak flow values. Multiple k-space lines per cardiac phase, $n_1 \geq 2$, are commonly applied in 4D flow MRI to shorten the inherent long scan times. We demonstrate that 2DRF 4D flow with $n_1 \geq 2$ can be easily combined with UNFOLD (UNaliasing by Fourier-encoding the Overlaps using the temporaL Dimension), a technique that allows regaining nominally the temporal resolution of the respective acquisition with $n_1 = 1$, to assure peak flow quantification.

Methods: Two different 2DRF pulses with spiral k-space trajectories were designed and integrated into a 4D flow sequence. Flow phantom experiments and 7 healthy control 4D flow in vivo measurements, with and without UNFOLD reconstructions, were compared with conventional reconstruction and 1D slab-selective excitation (1DRF) by evaluating time-resolved flow curves, peak flow, peak velocity, blood flow volume per cardiac cycle, and spatial aliasing.

Results: Applying UNFOLD to 4D flow imaging with 2DRF and reduced FOV increased the quantified in vivo peak flow values significantly by $3.7\% \pm 2.3\%$ to $5.2\% \pm 2.4\%$ ($P < .05$). Accordingly, the peak flow underestimation of 2DRF scans compared with conventional 1DRF scans decreased with UNFOLD. Finally, 2DRF combined with UNFOLD accelerated the 4D flow acquisition 3.5 ± 1.4 fold by reducing the FOV and increasing the effective temporal resolution by 6.7% compared with conventional 1D selective excitation, with 2 k-space lines per cardiac phase.

Conclusion: Two-dimensional selective excitation combined with UNFOLD allows limiting the FOV to shorten 4D flow scan times and compensates for the loss in temporal resolution with 2DRF ($\Delta t = 64.8$ ms) compared with 1DRF ($\Delta t = 43.2$ ms), yielding an effective resolution of $\Delta t_{\text{eff}} = 40.5$ ms to enhance peak flow quantification.

This is an open access article under the terms of the Creative Commons Attribution License, which permits use, distribution and reproduction in any medium, provided the original work is properly cited.

© 2019 The Authors Magnetic Resonance in Medicine published by Wiley Periodicals, Inc. on behalf of International Society for Magnetic Resonance in Medicine

KEYWORDS

4D flow, fast imaging, reduced FOV, reduced FOX, spatially selective 2D RF excitation, UNFOLD

1 | INTRODUCTION

Temporally resolved, complex, 3D velocity vector fields can be measured noninvasively by 4D flow imaging¹ to characterize hemodynamics, for example in intracranial aneurysms or feeding arteries of arteriovenous malformations.^{2,3} In stenotic diseases, it has been shown that, in particular, the peak flow decreases significantly and may therefore serve as a biomarker.^{4,5} Still, long acquisition times of 10–20 minutes prevent the routine clinical application of 4D flow imaging,¹ even though multiple k-space lines per cardiac phase, $n_1 \geq 2$, are typically acquired.¹ Therefore, 4D flow MRI has been accelerated by various spatial and temporal undersampling techniques.^{6–11}

Another promising acceleration approach restricts the field of excitation (FOX) in 2D by using 2D spatially selective excitation (2DRF), which allows reducing the FOV in 2D to the target region only.^{12–14} Spatial selectivity is achieved by applying gradients along both selective directions during RF application using, for example, a spiral excitation-k-space trajectory. Recently, 2DRF has been applied successfully to accelerate 4D flow imaging (2DRF 4D flow),¹⁵ and 2DRF 4D flow reduced scan times from 23.6 ± 4.7 minutes to 6.7 ± 1.3 minutes. However, 2DRF pulse durations of about 3.5 ms reduced the temporal resolution compared with conventional 1-dimensional (1D) slab-selective RF pulses (1DRF, such as SINC).¹⁵ The temporal resolution is, however, critical for correct peak flow quantification.^{16–18} Furthermore, the reduced FOV (rFOV) needs to be oversampled in both phase-encoding directions¹⁹ (i.e., rFOV > FOX), to prevent *static* spatial aliasing,¹⁹ which prolongs the scan time.

UNaliasing by Fourier-encoding the Overlaps using the temporal Dimension (UNFOLD) (20, 21) is a dynamic acceleration technique that retrospectively increases the temporal resolution of an originally segmented k-space acquisition.¹⁹ The UNFOLD technique has been applied successfully to cardiac imaging,^{20,21} MR thermometry,^{19,22} and functional MRI²⁰ for dedicated reconstructions of phase-contrast MRI²³ and to 4D flow MRI as shown in initial results.¹¹ Despite the technique's benefits, UNFOLD may induce *dynamic* spatial aliasing.¹⁹ However, the combination of 2DRF and UNFOLD mitigates UNFOLD's intrinsic risk of *dynamic* aliasing by using spatial oversampling, which is needed for 2DRF to avoid *static* aliasing, as shown in phantom and in vivo abdominal imaging.¹⁹

In this work, we investigate the benefit of an UNFOLD-2DRF combination for 4D flow imaging. Because 4D flow MRI is commonly acquired with $n_1 \geq 2$ to shorten scan durations, UNFOLD may be readily applied. The combination

is expected to (1) accelerate 1DRF 4D flow by reducing the FOV, (2) regain the temporal resolution of a respective 1DRF acquisition with $n_1 = 2$ by applying UNFOLD to assure peak flow quantification,¹⁶ and (3) diminish dynamic and static aliasing by combining 2DRF and UNFOLD.

The UNFOLD 2DRF 4D flow sequence is tested in pulsatile flow phantom and in vivo measurements. Time-resolved flow curves, velocity curves, and magnitude and velocity images are calculated to investigate the method's excitation, reconstruction, and aliasing behavior. Two different UNFOLD filter bandwidths and 2DRF pulses are evaluated with respect to peak flow quantification, peak velocity, flow volume per cardiac cycle, and aliasing behavior, and compared with reconstructions without UNFOLD. Here, the time sensitivity of 4D flow enables investigating the temporal reconstruction accuracy of UNFOLD. Furthermore, peak flow quantified when applying 2DRF excitation with and without UNFOLD is compared with 1DRF-excitation. Finally, SNR is investigated for different 2DRF excitation and UNFOLD reconstruction types.

2 | METHODS

2.1 | Two-dimensional selective excitation

The small-tip angle model¹² was used to design 2 different 2DRF pulses described in detail in Wink et al.¹⁵ Briefly, the first pulse, RFL, excites a rectangular bar with FOX = ($\infty \times 6 \times 6$) cm³ and bandwidth-time product (BWTP) = 1.2, and the second, RFS, excites a smaller FOX = ($\infty \times 3.6 \times 3.6$) cm³ with BWTP = 0.9. Both 3.5-ms-long pulses were calculated in MATLAB (MathWorks, Natick, Massachusetts) based on spiral k-space trajectories located in the k_y, k_z -plane orthogonal to the nonselective k_x -axis. The measured gradient waveforms²⁴ were integrated in the RF-pulse calculations to improve the excitation profile.¹⁵

Both 2DRF pulses were integrated into a prospectively electrocardiogram-triggered Cartesian 4D flow sequence,^{1,25} such that the readout was oriented along the nonselective axis.

2.2 | Flow phantom experiments

Flow phantom experiments were performed on a 3T scanner (Magnetom Verio; Siemens, Erlangen, Germany) using a 15-channel knee coil. The phantom consisted of an outer cylindrical bottle of 112-mm diameter and 2 inner tubes of 16-mm diameter,¹⁵ which were connected to a pulsatile flow pump (CardioFlow 5000 MR; Shelley Medical Imaging

Technologies, London, Canada) (Supporting Information Figure S1). Distilled water was flowing forward in the right tube and backward in the left tube, mimicking pulsatile blood flow with a maximal flow rate of 170 mL/s using the vendor's carotid flow curve. The 4D flow acquisitions with rFOV were performed (1) with RFL and the rFOV adjusted to the FOX of RFL (FOVL) = $128 \times 96 \times 96 \text{ mm}^3$, and (2) with RFS and the rFOV adjusted to the FOX of RFS (FOVS) = $128 \times 64 \times 64 \text{ mm}^3$, each with $n_1 = 1$ and $n_1 = 2$. (3) For reference, 4D flow was obtained with 1DRF excitation in a full FOV of $128 \times 128 \times 96 \text{ mm}^3$, using $n_1 = 1$ and $n_1 = 2$. All phantom acquisition parameters are given in Table 1A.

2.3 | In vivo acquisition

Three 4D flow scans targeting the circle of Willis, the internal carotid arteries (ICAs), and the basilar artery were each acquired in 7 healthy volunteers (age: 33.7 ± 12.5 years, 3 females, 4 males) on the previously mentioned 3T system using a 12-channel head coil and a vendor-provided electrocardiogram for prospective cardiac triggering. Written informed consent was obtained from the subjects according to a local institutional review board–approved protocol. The first 2 scans were performed using (I) RFL with FOVL and (II) RFS with FOVS, orienting the nonselective readout axis in the right–left direction. The third scan (III) with 1DRF served as the reference and was oriented as in data sets (I) and (II). Its FOV was adjusted in the first phase-encode (PE1) direction to the subject's head size, resulting in the full FOV of $(256 \times 222 \pm 18 \times 96) \text{ mm}^3$. All in vivo scans were acquired with $n_1 = 2$ and acquisition times of (I) 15.5 ± 3.7 minutes, (II) 6.7 ± 1.3 minutes, and (III) 35.4 ± 7.0 minutes. Table 1B summarizes all in vivo acquisition parameters.

Residual background phase, for example, due to eddy currents, was corrected using a first-order polynomial fit to the phase difference in static tissue. Distortion and concomitant fields were not corrected for, as 2D-selective excitations were performed in isocenter and flow analysis was performed maximally ± 2 cm from isocenter. Noise, static tissue, and vessels were segmented semi-automatically¹⁵ with fuzzy c-means clustering^{26–28} and Otsu's thresholding.²⁹

2.4 | Reconstruction with UNFOLD

All data reconstruction and postprocessing was performed in MATLAB. To increase the temporal resolution, data sets acquired with $n_1 = 2$ were reconstructed with an UNFOLD factor of 2 (UNFOLD2). In UNFOLD2, odd and even k-space lines of each cardiac phase are split into 2 separate time frames (Supporting Information Figure S2A), which doubles the *nominal* temporal resolution and halves the

number of k-space lines, resulting in undersampling artifacts (Supporting Information Figure S2B). Consequently, the k-space sets of adjacent time frames are shifted by half a line; therefore, first-order aliasing artifacts toggle their phase by 180° . The UNFOLD technique^{19,20} removes the undersampling artifacts by applying a fast Fourier transform along the temporal dimension and a Fermi filter $f(E) = (1 + \exp(\beta(|E| - E_f)))^{-1}$ in the resulting temporal frequency space (Supporting Information Figure S2C). Here, we used $\beta^{-1} = 0.022N_y$, based on Madore et al,²⁰ and compared $E_f = 0.5N_y$ and $E_f = 0.8N_y$ regarding SNR and peak flow quantification (E , frequency; N_y , Nyquist frequency). Because $f(E)$ is a low-pass filter, the threshold E_f yields the *effective* temporal resolution and artifact level. Finally, the unaliased images were obtained by applying an inverse fast Fourier transform in time (Supporting Information Figure S2D). Dynamic aliasing may occur if the dynamic bandwidth of the data is larger than E_f . If UNFOLD is combined with 2DRF, it occurs at the rFOV borders, which have been acquired sparsely to prevent static aliasing. Whereas the *nominal* temporal resolution is always doubled with UNFOLD2, the *effective* temporal resolution Δt_{eff} is controlled by E_f . With nominal $\Delta t = 32.4$ ms, $E_f = 0.5N_y$ results in $\Delta t_{\text{eff}} = 64.8$ ms, and $E_f = 0.8N_y$ yields $\Delta t_{\text{eff}} = 40.5$ ms.

2.5 | Evaluation of UNFOLD reconstruction

2.5.1 | Flow phantom experiments

The time-resolved flow $Q(t)$ ¹⁵ was determined within the right tube cross section and eventually after UNFOLD2 reconstruction of the corresponding RFL and RFS data sets. To analyze dynamic aliasing due to UNFOLD, magnitude and velocity images were investigated at peak flow. Additionally, the differences in peak flow \hat{Q} between $n_1 = 2$ data sets and $n_1 = 1$ data sets were calculated for RFL and RFS and for the different reconstruction types.

2.5.2 | In vivo acquisition

To evaluate the image quality for all 4 combinations of 1DRF/2DRF acquisitions reconstructed without/with UNFOLD while matrix sizes and acquisition times are kept similar, data sets (I) and (II) were 2-fold undersampled for UNFOLD reconstruction, termed (I^{2x}) and (II^{2x}), and reconstructed both without and with UNFOLD ($E_f = 0.5N_y$). Furthermore, data set (III) was retrospectively 4-fold undersampled in the PE1-direction (data set III^{4x}) to match approximately data set (I^{2x}) and 6-fold undersampled (data set III^{6x}) to match approximately data set (II^{2x}) in both matrix size and acquisition time. Both data sets (III^{4x}) and (III^{6x}) were reconstructed without and with UNFOLD.

TABLE 1 Acquisition parameters

(A) Acquisition parameters of phantom measurements											
Scan	Matrix ^a	FOV (mm ³) ^a	TR/ Δt (ms)	TE (ms)	RF pulse	# Seg-ments	Flip angle	Coil ^b	Venc (m/s)	# Time frames	Acq. time (min:s)
(i.1)	(64 × 48 × 48)	(128 × 96 × 96)	8.1/32.4	2.8	RFL	1	6°	15 (knee)	1	24	30:43
(i.2)	(64 × 48 × 48)	(128 × 96 × 96)	8.1/64.8	2.8	RFL	2	6°		1	8 ^c	15:22
(ii.1)	(64 × 32 × 32)	(128 × 64 × 64)	8.1/32.4	2.8	RFS	1	6°		1	23	13:03
(ii.2)	(64 × 32 × 32)	(128 × 64 × 64)	8.1/64.8	2.8	RFS	2	6°		1	12	6:50
(iii.1)	(64 × 64 × 48)	(128 × 128 × 96)	5.4/21.6	3.2	1DRF ^d	1	6°		1	37	40:58
(iii.2)	(64 × 64 × 48)	(128 × 128 × 96)	5.4/43.2	3.2	1DRF ^d	2	6°		1	18	20:29
(B) Acquisition parameters of in vivo study											
Scan	Matrix ^a	FOV (mm ³) ^a	TR/ Δt (ms)	TE (ms)	RF pulse	# Seg-ments	Flip angle	Coil ^b (# channels)	Venc (m/s)	Cardiac phases ^e	Acq. time (min:s) ^f
(I)	(128 × 48 × 48)	(256 × 96 × 96)	8.1/64.8	2.8	RFL	2	5°	12 (head)	1	12.4 ± 3.0	15:28 ± 3:40
(II)	(128 × 32 × 32)	(256 × 64 × 64)	8.1/64.8	2.8	RFS	2	5°		1	12.1 ± 2.4	6:43 ± 1:18
(III)	(128 × 111 ± 9 × 48) ^g	(256 × 222 ± 18 × 96) ^g	5.4/43.2	3.2	1DRF ^d	2	5°		1	18.3 ± 3.5	35:23 ± 6:59

Note: Matrix and FOV are given in the format RO × PE1 × PE2.

Abbreviations: acq., acquisition; min:s, minutes:seconds; Venc, maximal encoding velocity.

^a2-mm isotropic resolution.

^bTransmit: birdcage body coil; receive: local receive arrays.

^cOnly the first 8 systolic out of 12 possible time frames were acquired.

^dSINC BWTP = 6; duration = 0.8 ms.

^eAdjusted to the subject's heartbeat.

^fVaries with individual FOV and cardiac phases.

^gAdjusted to the subject's head size.

Blood velocity $v(t)$ and flow $Q(t)$ were determined within a cross section of the subject's ICAs, basilar artery, and middle cerebral arteries (MCAs).¹⁵ To investigate temporal resolution effects, $v(t)$ and $Q(t)$ were calculated for acquisitions (I) and (II), reconstructed without and with UNFOLD ($E_f = 0.5N_y$ and $E_f = 0.8N_y$) and for reference data (III).

Moreover, the difference in systolic peak flow $\Delta\hat{Q} = \hat{Q} - \hat{Q}_{\text{ref}}$ and peak velocity $\Delta\hat{v} = \hat{v} - \hat{v}_{\text{ref}}$ between data sets (I) or (II) and the reference (III), the differences $\Delta\hat{Q} = \hat{Q}_{\text{UNFOLD}} - \hat{Q}_{\text{ref}}$ and $\Delta\hat{v} = \hat{v}_{\text{UNFOLD}} - \hat{v}_{\text{ref}}$ between the UNFOLD reconstructed data sets (I) or (II) and the reference (III), and the difference $\Delta\hat{Q}_{\text{UNFOLD}} = \hat{Q}_{\text{UNFOLD}} - \hat{Q}$ between reconstruction with and without UNFOLD of data sets (I) and (II) were determined. Here, both UNFOLD reconstructions using $E_f = 0.5N_y$ and $E_f = 0.8N_y$ were investigated.

To investigate the UNFOLD reconstruction accuracy during diastole, the blood-flow volume per cardiac cycle V^{15} was determined, and the difference ($\Delta V_{\text{UNFOLD}} = V_{\text{UNFOLD}} - V$) between reconstruction without (V) and with UNFOLD (V_{UNFOLD}) was computed for data sets (I) and (II).

Differences, mean differences ($\Delta\hat{Q}$, $\Delta\hat{Q}_{\text{UNFOLD}}$, $\Delta\hat{v}$, and ΔV_{UNFOLD}), and SDs across all subjects were visualized in Bland-Altman plots. Statistical analysis was performed using first Lilliefors test to confirm that V and \hat{Q} were normally distributed across subjects, and consequently a t-test to determine P values.

2.5.3 | Signal-to-noise ratio

The average SNR within static tissue was determined based on Constantinides et al.³⁰ following the root sum squared combination of the individual receiver coils in each volunteer for all 9 combinations of different acquisition and reconstruction types. The mean magnitude signal \overline{M}_s was computed within static tissue segments, whereas the mean noise magnitude \overline{M}_n was computed within noise segments. Finally, $\text{SNR} = \overline{M}_s / \overline{M}_n$ and relative SNR were calculated. Mean values and SDs were calculated over all subjects, and if applicable over reconstruction or excitation types.

3 | RESULTS

3.1 | Flow phantom experiments

Using $n_1 = 2$ instead of $n_1 = 1$, as used for reference, the peak flow was reduced by -2.9% (RFL, Figure 1A) and -2.6% (RFS, Figure 1B). Reconstructing these data sets using UNFOLD2 with $E_f = 0.5N_y$, the underestimation in peak flow was reduced to -0.2% (RFL) and $+0.6\%$ (RFS), despite using a low effective temporal resolution with $\Delta t_{\text{eff}} = 64.8$ ms. Applying

UNFOLD2 with $\Delta t_{\text{eff}} = 40.5$ ms, peak flow underestimation was reduced to -1.2% (RFL) and -0.6% (RFS). Whereas no dynamic aliasing was visible when applying UNFOLD with $E_f = 0.5N_y$, dynamic aliasing appeared during systole close to the rFOV boundary when applying UNFOLD with the broad frequency filter $E_f = 0.8N_y$ (Figure 1, white arrows). Moreover, 2DRF reference data sets with $n_1 = 1$ coincide well with 1DRF data sets with both $n_1 = 1$ and $n_1 = 2$ (Figure 1C-F).

3.2 | In vivo study

The 2D selective excitation with rFOV was qualitatively successful without visible aliasing (Supporting Information Figure S3B,H). Whereas the longer 2DRF-pulse duration decreased the temporal resolution by 33% compared with 1DRF excitation, UNFOLD retrospectively doubled the 2DRF temporal resolution nominally. Furthermore, UNFOLD effectively removed the aliasing in data sets (I^{2x}) and (II^{2x}) near the rFOV borders, resulting in image quality equivalent to conventional data sets (I) and (II) (Supporting Information Figure S3F,L).

Time-resolved flow curves through the ICAs of 2DRF data sets (I) and (II), reconstructed without ($\Delta t = 64.8$ ms) and with UNFOLD ($\Delta t = 32.4$ ms) were observed to be qualitatively similar during cardiac phases with slowly varying flow for all volunteers (Figure 2 and Supporting Information Figure S4). Accordingly, mean deviations in flow volume per cycle between reconstructions with and without UNFOLD ΔV_{UNFOLD} were close to zero using both RFL and RFS (Figure 3D). For RFL, no significant difference was found for both $E_f = 0.5N_y$ and $E_f = 0.8N_y$, whereas for RFS the deviation in flow volume per cycle was significant ($P < .05$).

However, during systole when flow rapidly changes, higher peak flow and peak velocities were observed with than without UNFOLD (Figures 2 and 3). Both 2DRF data sets (I and II) without UNFOLD underestimated peak flow compared with data set (III) (Figure 3A, top). Applying UNFOLD to the 2DRF data sets (I and II), the mean peak flow deviation decreased (Figure 3A, bottom). In none of the cases significant differences were found between the data sets, although differences were smaller for RFL. Still, P -values increased when using UNFOLD (Table 2A). Similarly, significantly higher peak flow was quantified with than without UNFOLD ($P < .05$), and the quantified peak flow increased with increasing E_f (Figure 3C). In conclusion, the increased temporal resolution due to UNFOLD allowed the peak flow of the 2DRF data sets (I and II) to converge toward the 1DRF reference (III) or even exceed data set (III) for $E_f = 0.8N_y$ and data set (I). Similarly, the mean peak velocity increased for data sets (I) and (II) by applying UNFOLD (Figure 3B and Table 2B).

Table 2 summarizes the mean differences in peak flow, peak velocity, and flow volume per cycle, and Supporting

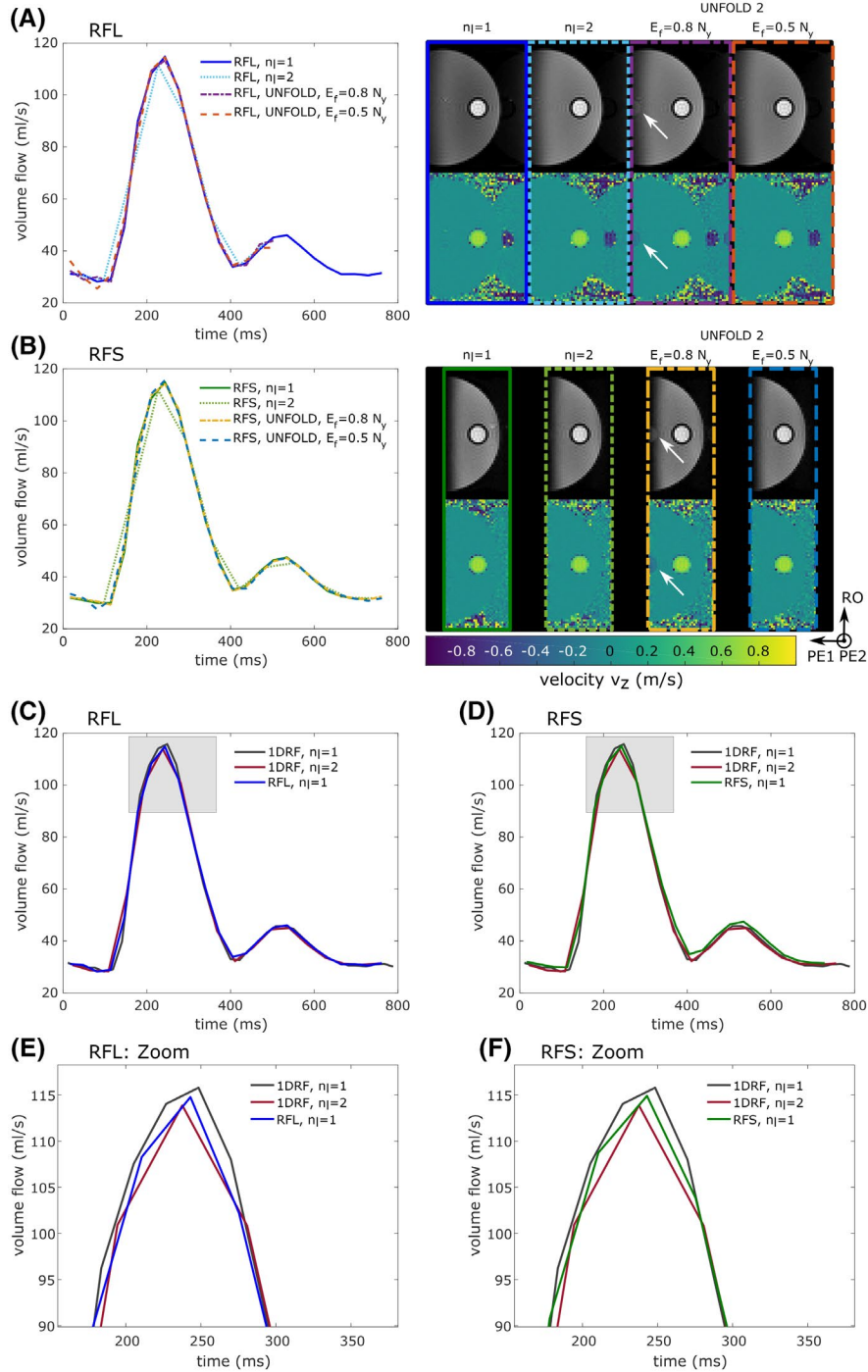
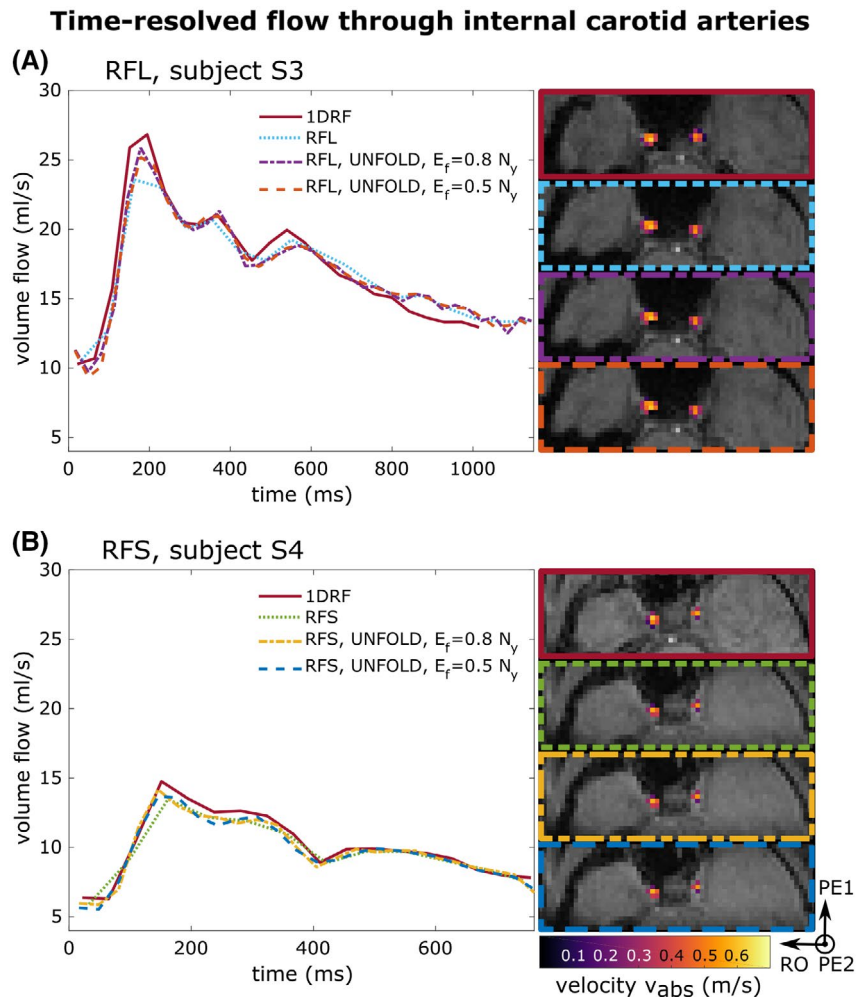


FIGURE 1 Time-resolved volume flow curves, $Q(t)$, of pulsatile flow in a flow phantom, and, A,B (right), systolic magnitude (gray) and velocity images (color) in flow direction, v_z . The respective 4D flow data were acquired using, A, the 2D selective excitation (2DRF) pulse, RFL, exciting a large field of excitation (FOX) = $(\infty \times 6 \times 6)$ cm³ with bandwidth time product (BWTP) = 1.2, and, B, the 2DRF pulse, RFS, exciting the small FOX = $(\infty \times 3.6 \times 3.6)$ cm³ with BWTP = 0.9, with 1 k-space line per cardiac phase ($n_1 = 1$; solid lines) or $n_1 = 2$ (nonsolid lines). The acquisitions with $n_1 = 2$ were reconstructed without UNFOLD (UNaliasing by Fourier-encoding the Overlaps using the temporaL Dimension; dotted lines) or using UNFOLD2, applying a Fermi filter with $E_f = 0.8 N_y$ (dash-dotted lines) or $E_f = 0.5 N_y$ (dashed lines). Although peak flow is underestimated using $n_1 = 2$ compared with $n_1 = 1$ by 2.9% (RFL) and 2.6% (RFS), it coincides well with the $n_1 = 1$ reference, applying UNFOLD2 with $E_f = 0.5 N_y$ (RFL, -0.2%; RFS, +0.6%) or $E_f = 0.8 N_y$ (RFL, -1.2%; RFS, -0.6%). White arrows indicate dynamic aliasing in systole due to the application of UNFOLD with a broad time-frequency filter ($E_f = 0.8 N_y$). C,D, Flow curves acquired using RFL (blue solid line) (C) and RFS (green solid line) (D) with $n_1 = 1$ agree well with the flow curves acquired using 1-dimensional (1D) slab-selective excitation (1DRF) and $n_1 = 1$ (gray solid line) or $n_1 = 2$ (dark red solid line). E,F, Zoomed-in view of the flow curves shown in (C) and (D) into the area highlighted as a gray rectangle. Abbreviations: PE1, phase-encode 1; PE2, phase-encode 2; RO, readout

FIGURE 2 Time-resolved volume-flow curves, $Q(t)$, through the internal carotid arteries obtained by 1DRF data (III) (solid, dark red line) and 2D selective, A, RFL data (I) reconstructed without (dotted light blue line) and with UNFOLD and Fermi filter with $E_f = 0.8N_y$ (dash-dotted purple line) and $E_f = 0.5N_y$ (dashed red line) and, B, RFS data (II) reconstructed without (dotted green line) and with UNFOLD and $E_f = 0.8N_y$ (dash-dotted yellow line) and $E_f = 0.5N_y$ (dashed blue line). The magnitude images with overlaid absolute velocity values in the right column show a zoomed-in view of the internal carotid arteries in the compared slices



Information Figure S4 shows time-resolved flow curves of all subjects S1-S7 in the ICA. Supporting Information Table S1 summarizes the respective relative mean differences in the ICA, basilar artery, and left and right MCA.

3.3 | Signal-to-noise ratio

Supporting Information Figure S5A shows the SNR relative to reference data set (III) without UNFOLD reconstruction. Compared to reconstruction without UNFOLD, the SNR augmented by $2.2\% \pm 0.1\%$ using UNFOLD with $E_f = 0.5N_y$, and decreased by $-18.9\% \pm 1.1\%$ using UNFOLD with $E_f = 0.8N_y$, independently of the excitation (Supporting Information Figure S5B). Compared with the 1DRF data set (III), the SNR increased by $8.6\% \pm 0.1\%$ with the RFL data set (I) and decreased by $-34.0\% \pm 0.9\%$ with RFS data set (II) independently of the reconstruction (Supporting Information Figure S5C). The findings suggest that excitation and reconstruction-based SNR changes are separable.

4 | DISCUSSION

In this work, we demonstrate the potential of UNFOLD to enhance peak flow quantification in 2DRF 4D flow by improving the temporal resolution $\Delta t = 64.8$ ms in 2DRF 4D flow to nominally $\Delta t = 32.4$ ms and effectively $\Delta t_{eff} = 40.5$ ms. Two different 2DRF pulses, RFS and RFL, in combination with UNFOLD2, were studied.

Although the benefit of combining 2DRF with UNFOLD¹⁹ and initial results applying UNFOLD to 4D flow¹¹ have been shown separately, we demonstrate here the synergy of combining UNFOLD and 2DRF for 4D flow. Because multiple k-space lines per cardiac phase (n_l) are commonly acquired in 4D flow MRI to keep scan durations short,¹ UNFOLD may be readily applied. Combining 2DRF and UNFOLD alleviates UNFOLD's inherent risk of dynamic aliasing by using spatial oversampling, which is required for 2DRF to prevent static aliasing.¹⁹ Combining all 3 techniques accelerates 4D flow by reducing the FOV, while regaining the temporal resolution of a respective 1DRF acquisition with $n_l = 2$ due to UNFOLD, and mitigates static and dynamic aliasing by the combination of 2DRF and UNFOLD.

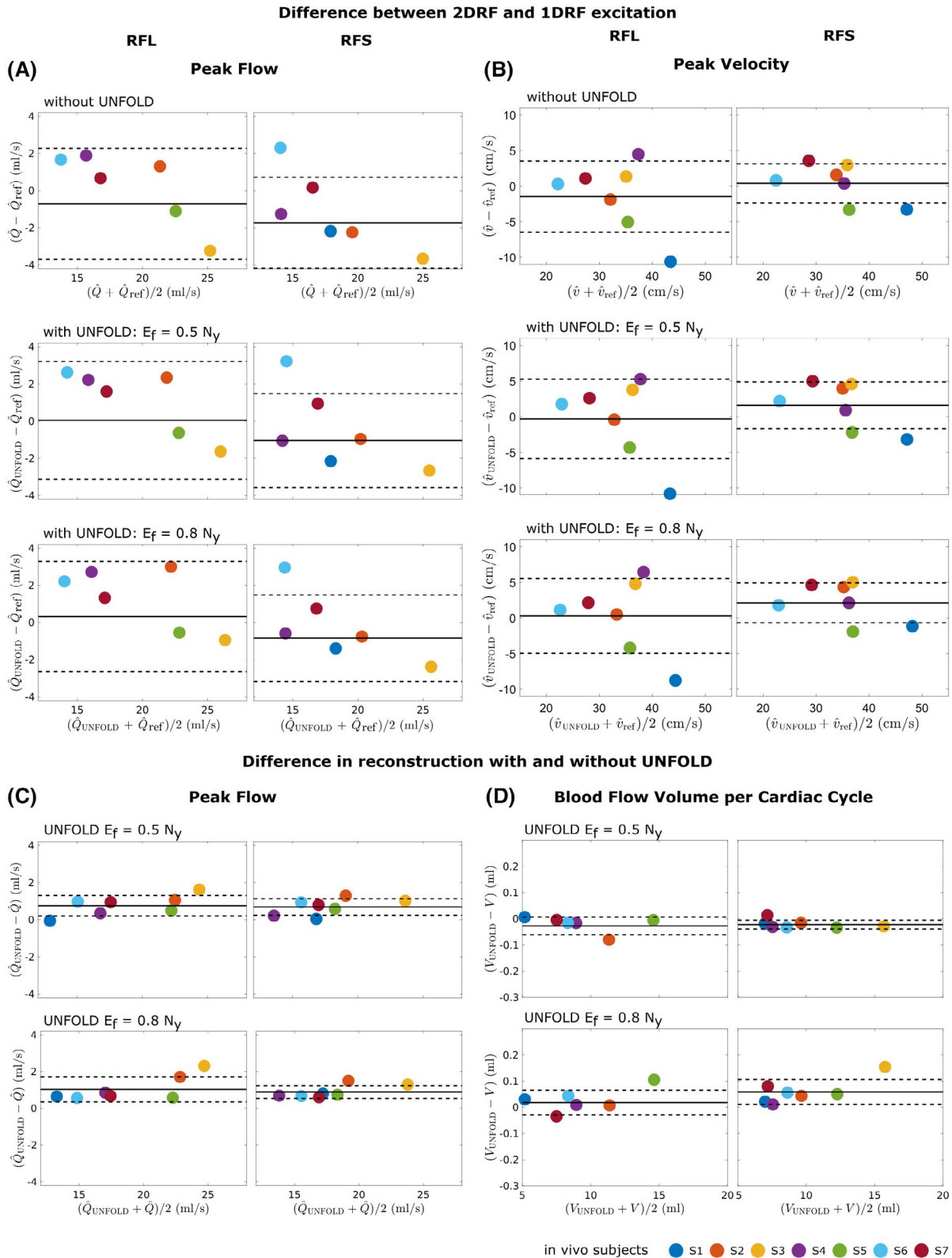


FIGURE 3 Bland-Altman plots analyzing the in vivo peak flow, peak velocity, and blood-flow volume per cardiac cycle for 2D selective excitations RFL (first subcolumn) and RFS (second subcolumn). Differences in peak flow \hat{Q} (A) and peak velocity \hat{v} (B) obtained with 2D selective excitations RFL or RFS in comparison to 1DRF ($\Delta t = 43.2$ ms). A,B, The 2DRF data were reconstructed without UNFOLD ($\Delta t = 64.8$ ms, first row) or with UNFOLD ($\Delta t = 32.4$ ms) using $E_f = 0.5 N_y$ (second row) or $E_f = 0.8 N_y$ (third row). C,D, Differences in 2DRF data reconstructed with and without UNFOLD regarding peak flow \hat{Q} (C) and blood-flow volume per cardiac cycle V (D). C,D, The UNFOLD technique was applied using $E_f = 0.5 N_y$ (first row) or $E_f = 0.8 N_y$ (second row). Solid lines indicate the mean deviation in peak flow, peak velocity, and flow volume per cardiac cycle, whereas dashed lines indicate the respective SD

TABLE 2 Mean differences in in vivo peak flow, peak velocity, and blood-flow volume per cardiac cycle between different excitation and reconstruction schemes

(A) Mean difference in in vivo peak flow between 1DRF excitation and 2DRF excitations RFL or RFS. 2DRF acquisitions were reconstructed without UNFOLD (line 1) or with UNFOLD with $E_f = 0.5 N_y$ (line 2) or $E_f = 0.8 N_y$ (line 3).		
2DRF	Mean difference in peak flow $\Delta\hat{Q} = \hat{Q}_{2DRF} - \hat{Q}_{ref}$ (mL/s)	
	RFL	RFS
without UNFOLD	-0.7 ± 3.0	-1.7 ± 2.5
with UNFOLD $E_f = 0.5N_y$	$+0.0 \pm 3.2$	-1.0 ± 2.6
with UNFOLD $E_f = 0.8N_y$	$+0.3 \pm 3.0$	-0.8 ± 2.3
2DRF	P-values	
	RFL	RFS
without UNFOLD	.553	.110
with UNFOLD $E_f = 0.5N_y$.971	.316
with UNFOLD $E_f = 0.8N_y$.784	.373
(B) Mean difference in in vivo peak velocity between 1DRF excitation and 2DRF excitations RFL or RFS. 2DRF acquisitions were reconstructed without UNFOLD (line 1) or with UNFOLD with $E_f = 0.5 N_y$ (line 2) or $E_f = 0.8 N_y$ (line 3).		
2DRF	Mean difference in peak velocity $\Delta\hat{v} = \hat{v}_{2DRF} - \hat{v}_{ref}$ (cm/s)	
	RFL	RFS
without UNFOLD	-1.5 ± 5.0	$+0.4 \pm 2.8$
with UNFOLD $E_f = 0.5N_y$	-0.3 ± 5.6	$+1.6 \pm 3.3$
with UNFOLD $E_f = 0.8N_y$	$+0.3 \pm 5.3$	$+2.1 \pm 2.8$
(C) Mean difference in in vivo peak flow between reconstruction without and with UNFOLD with $E_f = 0.5 N_y$ (line 1) or $E_f = 0.8 N_y$ (line 2) for 2DRF excitations RFL and RFS.		
2DRF	Mean difference in peak flow $\Delta\hat{Q} = \hat{Q}_{UNFOLD} - \hat{Q}$ (mL/s)	
	RFL	RFS
with UNFOLD $E_f = 0.5N_y$	0.75 ± 0.55^a	0.68 ± 0.45^a
with UNFOLD $E_f = 0.8N_y$	1.03 ± 0.69^a	0.88 ± 0.35^a
(D) Mean difference in in vivo blood-flow volume per cardiac cycle between reconstruction without and with UNFOLD with $E_f = 0.5 N_y$ (line 1) or $E_f = 0.8 N_y$ (line 2) for 2DRF excitations RFL and RFS.		
2DRF	Mean difference in blood-flow volume $\Delta\hat{V} = \hat{V}_{UNFOLD} - \hat{V}$ (mL)	
	RFL	RFS
with UNFOLD $E_f = 0.5N_y$	-0.03 ± 0.04	-0.02 ± 0.02^a
with UNFOLD $E_f = 0.8N_y$	$+0.02 \pm 0.05$	$+0.06 \pm 0.05^a$

^a $P \leq .05$.

Applying RFS in vivo allowed reducing the FOV and thus the scan time by $-71\% \pm 9\%$, but the temporal resolution decreased by 33.3% due to the 3.5-ms pulse duration of the 2DRF pulses. Applying UNFOLD2 with $E_f = 0.8N_y$ increased the nominal temporal resolution by 33.3% and the effective temporal resolution by 6.7%, both compared to the 1DRF reference with $n_1 = 2$. Keeping this increase in temporal resolution, FOV and scan time could be maximally reduced 4.5-fold¹⁵ with this technique. In this work, the *nominal* temporal resolution refers to the temporal spacing between UNFOLD undersampled k-space sets. The maximally resolvable temporal variation, however, is given by the UNFOLD Fermi filter E_f and the resulting *effective* temporal resolution.

The 4D flow imaging with 2DRF yielded significantly higher in vivo peak flow values when applying UNFOLD as compared with peak flow values obtained without UNFOLD ($P < .05$). Without UNFOLD and with 2DRF, instead of 1DRF excitation, peak flow was underestimated due to the lower temporal resolution.¹⁷ Applying UNFOLD, peak flow underestimation decreased. Similarly, the quantified peak velocity increased by applying UNFOLD. Likewise, peak velocity and flow in the basilar artery and both middle cerebral arteries increased when applying UNFOLD, whereas the blood flow volume remained constant.

Flow phantom experiments confirmed such findings. Notably, even using UNFOLD2 with $E_f = 0.5N_y$ (i.e., changing only the *nominal*, but not the *effective* temporal resolution) improved peak flow quantification. Additionally, flow phantom experiments for UNFOLD3 reconstruction were performed and yielded similar results as UNFOLD2 experiments. Dynamic aliasing appeared when using UNFOLD with 1.6-fold the acquisition bandwidth ($E_f = 0.8N_y$). For UNFOLD2, it appeared at the FOV borders only, which were oversampled to prevent static aliasing from residual excitation and may be discarded. The static aliasing in the 2-fold undersampled in vivo data sets (I^{2x} and II^{2x}) at the rFOV boundaries (Supporting Information Figure S3D,J, white arrows) indicates where dynamic aliasing may potentially occur. Keeping acquisition and UNFOLD bandwidth the same, no dynamic aliasing occurred.

The SNR appeared to depend on acquisition and reconstruction type separately. Acquisition-wise, the SNR increased for the RFL compared with the 1DRF data, whereas it was expected to decrease by -25.5% due to changes in number of k-space lines, TR, TE, and assuming $T_1 = 1084 \text{ ms}^{31}$ and a flip angle (FA) of 5° . The observed changes in SNR could be explained by actual FAs of 3° (1DRF) and 6° (RFL), which differ from the nominal FA of 5° . Reconstruction-wise, the SNR decreased using UNFOLD2 with $E_f = 0.8N_y$ by $-18.9\% \pm 1.1\%$, but increased for $E_f = 0.5N_y$ by $+2.2\% \pm 0.1\%$, as expected theoretically ($E_f = 0.8N_y$: -19.8% ; $E_f = 0.5N_y$: $+2.3\%$).²⁰

This study has several limitations. First, this work would profit from using higher FAs, to benefit from inflow effects. Here, FAs below the Ernst angle were used, which allowed us to verify the excitation pattern straightforwardly. Second, in addition to the reference measurements with 1DRF excitation and $n_1 = 1$, a flow meter as ground truth would strengthen the phantom results. Third, distortion and concomitant fields were not corrected for; however, 2D selective excitations were performed in isocenter and velocities were analyzed within ± 2 cm from isocenter. Furthermore, the spatial resolution of 2-mm isotropic may limit the quantification of hemodynamic parameters in the basilar artery, middle cerebral arteries, and internal carotid arteries, due to their small diameters in the range of 3–5 mm.^{32,33} Finally, a general limitation of our implementation was given by the effective temporal resolution of UNFOLD 2DRF 4D flow, which is limited to $\Delta t_{\text{eff}} > 4 \text{ TR} = 32.4$ ms. Still, typical temporal resolutions in 4D flow are $\Delta t = 40$ –50 ms, independent of the target region.¹

Ultimately, 2DRF excitation with UNFOLD2 permits quantifying peak flow successfully, filtering either with $E_f = 0.5N_y$, if this matches the flow signal bandwidth, or using $E_f > 0.5N_y$ and possibly halving the rFOV by discarding its boundaries to mitigate dynamic aliasing.

The presented method would be suitable, for example, for aortic scans, in which maximal accelerations of 25 m/s^2 have been measured at velocities of approximately 1 m/s at the aortic valve,³⁴ which translate to a velocity change with 25 Hz, matching the bandwidth of 24.7 Hz when using UNFOLD2 with $E_f = 0.8N_y$.

This study supports future 2DRF 4D flow imaging at ultrahigh fields, characterizing, for example, aneurysms or arteriovenous malformation with high spatio-temporal resolution. Furthermore, the joint technique might prove useful to reduce motion artifacts, such as swallowing artifacts³⁵ in carotid artery imaging, while preserving high temporal resolutions. Combining retrospective electrocardiogram triggering with compressed sensing, temporal resolutions with $\Delta t < 2 \text{ TR}$ have been shown for 2D cine phase-contrast MRI.³⁶ Similarly, integrating 2DRF pulses into a retrospectively electrocardiogram-triggered 4D flow sequence would allow reconstructing 2DRF 4D flow MRI with $\Delta t < 4 \text{ TR}$. Using parallel transmission^{37,38} to decrease 2DRF pulse durations³⁹ is another option to increase temporal resolutions, which would additionally decrease the excitation sensitivity to magnetic field inhomogeneities.

5 | CONCLUSIONS

This work addresses the challenge of limited temporal resolutions in 2DRF 4D flow imaging by applying UNFOLD, which allows maintaining temporal resolutions of effectively $\Delta t_{\text{eff}} = 40.5$ ms, to correctly quantify peak flow while

reducing the FOV to limit both scan time and potential motion artifacts. Considering that $n_1 = 2$ is often used in 4D flow MRI, UNFOLD reconstruction allows increasing the temporal resolution at low expenditure. In combination with 2D selective excitation, it becomes fully effective, as potential dynamic aliasing occurs in rFOV borders acquired to prevent static aliasing only.

ACKNOWLEDGMENTS

The Authors gratefully acknowledge co-funding from the German Research Foundation (GRK2260, BIOQIC and SCHM 2677/2-1).

ORCID

Clarissa Wink  <https://orcid.org/0000-0002-6547-4851>

Tobias Schaeffter  <https://orcid.org/0000-0003-1310-2631>

Sebastian Schmitter  <https://orcid.org/0000-0003-4410-6790>

REFERENCES

1. Markl M, Frydrychowicz A, Kozerke S, Hope M, Wieben O. 4D flow MRI. *J Magn Reson Imaging*. 2012;36:1015–1036.
2. Cecchi E, Giglioli C, Valente S, et al. Role of hemodynamic shear stress in cardiovascular disease. *Atherosclerosis*. 2011; 214:249–256.
3. Schnell S, Ansari SA, Vakil P, et al. Three-dimensional hemodynamics in intracranial aneurysms: influence of size and morphology. *J Magn Reson Imaging*. 2014;39:120–131.
4. Schoenberg SO, Knopp MV, Bock M, et al. Renal artery stenosis: grading of hemodynamic changes with cine phase-contrast MR blood flow measurements. *Radiology*. 1997;203:45–53.
5. Versluis B, Nelemans PJ, Wildberger JE, Schurink GW, Leiner T, Backes WH. Magnetic resonance imaging-derived arterial peak flow in peripheral arterial disease: towards a standardized measurement. *Eur J Vasc Endovasc Surg*. 2014;48:185–192.
6. Schmitter S, Schnell S, Ugurbil K, Markl M, Van de Moortele PF. Towards high-resolution 4D flow MRI in the human aorta using kt-GRAPPA and B1+ shimming at 7T. *J Magn Reson Imaging*. 2016;44:486–499.
7. Deng Z, Yang W, Pang J, et al. Improved vessel-tissue contrast and image quality in 3D radial sampling-based 4D-MRI. *J Appl Clin Med Phys*. 2017;18:250–257.
8. Pagé G, Bettoni J, Salsac AV, Balédent O. Influence of principal component analysis acceleration factor on velocity measurement in 2D and 4D PC-MRI. *Magn Reson Mater Phys Biol Med*. 2018;31:469–481.
9. Santelli C, Loecher M, Busch J, Wieben O, Schaeffter T, Kozerke S. Accelerating 4D flow MRI by exploiting vector field divergence regularization. *Magn Reson Med*. 2016;75:115–125.
10. Mazzoli V, Gottwald L, Peper E, et al. Accelerated 4D phase contrast MRI in skeletal muscle contraction. *Magn Reson Med*. 2018;80:1799–1811.
11. Braig M, Krafft AJ, Leupold J, Hennig J, Menza M, von Elverfeldt D. Evaluation of accelerated preclinical 4D-flow imaging with UNFOLD. In: Proceedings of the 25th Annual Meeting of ISMRM, Honolulu, Hawaii, 2017. p 4881.
12. Pauly J, Nishimura D, Macovski A. A k-space analysis of small-tip-angle excitation. *J Magn Reson*. 1989;81:43–56.

13. Nehrke K, Börnert P, Groen J, Smink J, Böck JC. On the performance and accuracy of 2d navigator pulses. *Magn Reson Imaging*. 1999;17:1173–1181.
14. Rieseberg S, Frahm J, Finsterbusch J. Two-dimensional spatially-selective RF excitation pulses in echo-planar imaging. *Magn Reson Med*. 2002;47:1186–1193.
15. Wink C, Ferrazzi G, Bassenge JP, et al. 4D flow imaging with 2D-selective excitation. *Magn Reson Med*. 2019;82:886–900.
16. Montalba C, Urbina J, Sotelo J, et al. Variability of 4D flow parameters when subjected to changes in MRI acquisition parameters using a realistic thoracic aortic phantom. *Magn Reson Med*. 2018;79:1882–1892.
17. Cibis M, Potters WV, Gijzen FJ, et al. The effect of spatial and temporal resolution of cine phase contrast MRI on wall shear stress and oscillatory shear index assessment. *PLoS ONE*. 2016;11:1–15.
18. Berg P, Stucht D, Janiga G, Beuing O, Speck O, Th'evenin D. Cerebral blood flow in a healthy circle of willis and two intracranial aneurysms: computational fluid dynamics versus four-dimensional phase-contrast magnetic resonance imaging. *J Biomech Eng*. 2014;136:041003.
19. Zhao L, Madore B, Panych LP. Reduced field-of-view MRI with two-dimensional spatially-selective RF excitation and UNFOLD. *Magn Reson Med*. 2005;53:1118–1125.
20. Madore B, Glover GH, Pelc NJ. Unaliasing by Fourier-encoding the overlaps using the temporal dimension (UNFOLD), applied to cardiac imaging and fMRI. *Magn Reson Med*. 1999;42:813–828.
21. Kellman P, Sorger JM, Epstein FH, McVeigh ER. Low latency temporal filter design for real-time MRI using UNFOLD. *Magn Reson Med*. 2000;44:933–939.
22. Mei C-S, Panych LP, Yuan J, et al. Combining two-dimensional spatially selective RF excitation, parallel imaging, and UNFOLD for accelerated MR thermometry imaging. *Magn Reson Med*. 2011;66:112–122.
23. Kerwin WS. High-pass-low-pass (HP-LP) reconstruction of CINE phase-contrast MRI. *Magn Reson Med*. 2004;52:566–574.
24. Duyn JH, Yang Y, Frank JA, van der Veen JW. Simple correction method for k-space trajectory deviations in MRI. *J Magn Reson*. 1998;132:150–153.
25. Markl M, Chan FP, Alley MT, et al. Time-resolved three-dimensional phase-contrast MRI. *J Magn Reson Imaging*. 2003;17:499–506.
26. Bezdek J. *Pattern Recognition With Fuzzy Objective Function Algorithms*. Berlin: Springer; 1981.
27. Sundareswaran KS, Frakes DH, Fogel MA, Soerensen DD, Oshinski JN, Yoganathan AP. Optimum fuzzy filters for phase-contrast magnetic resonance imaging segmentation. *J Magn Reson Imaging*. 2009;29:155–165.
28. Bock J. *Development and Testing of New Strategies for Pre-processing and Analysis of 4D Flow-Sensitive MRI Data*. Breisgau, Germany: Albert-Ludwigs-Universität Freiburg im Breisgau; 2013.
29. Otsu N. A threshold selection method from gray-level histograms. *IEEE Trans Syst Man Cybern*. 1979;9:62–66.
30. Constantinides CD, Atalar E, McVeigh ER. Signal-to-noise measurements in magnitude images from NMR phased arrays. *Magn Reson Med*. 1997;38:852–857.
31. Stanisz GJ, Odobina EE, Pun J, et al. T1, T2 relaxation and magnetization transfer in tissue at 3T. *Magn Reson Med*. 2005;54:507–512.
32. Smoker WR, Price MJ, Keyes WD, Corbett JJ, Gentry LR. High-resolution computed tomography of the basilar artery. 1: Normal size and position. *Am J Neuroradiol*. 1986;7:55–60.
33. Serrador JM, Picot PA, Rutt BK, Shoemaker JK, Bondar RL. MRI measures of middle cerebral artery diameter in conscious humans during simulated orthostasis. *Stroke*. 2000;31:1672–1678.
34. Barker AJ, Staehle F, Bock J, Jung BA, Markl M. Analysis of complex cardiovascular flow with three-component acceleration-encoded MRI. *Magn Reson Med*. 2012;67:50–61.
35. Bousset L, Herigault G, de la Vega A, Nonent M, Douek PC, Serfaty JM. Swallowing, arterial pulsation, and breathing induce motion artifacts in carotid artery MRI. *J Magn Reson Imaging*. 2006;23:413–415.
36. Peper ES, Strijkers GJ, Gazzola K, et al. Regional assessment of carotid artery pulse wave velocity using compressed sensing accelerated high temporal resolution 2D CINE phase contrast cardiovascular magnetic resonance. *J Cardiovasc Magn Reson*. 2018;20:86.
37. Katscher U, Börnert P, Leussler C, van den Brink JS. Transmit SENSE. *Magn Reson Med*. 2003;49:144–150.
38. Padormo F, Beqiri A, Hajnal JV, Malik SJ. Parallel transmission for ultrahigh-field imaging. *NMR Biomed*. 2016;29:1145–1161.
39. Wu X, Vaughan JT, Ugurbil K, Van de Moortele PF. Parallel excitation in the human brain at 9.4T counteracting k-space errors with RF pulse design. *Magn Reson Med*. 2010;63:524–529.

SUPPORTING INFORMATION

Additional supporting information may be found online in the Supporting Information section.

FIGURE S1 Illustration of the setup with flow phantom and the pulsatile flow pump (CardioFlow 5000 MR). The inlay shows a sketch of the flow phantom and the 2DRF pattern

FIGURE S2 Illustration of data processing with UNFOLD. A, The data of a sequence acquiring 2 k-space lines per cardiac phase were split into 2 separate phases. The set of k-space lines was then shifted by half a line from phase to phase. B, Every phase was Fourier-transformed to complex image space. The phase of the resulting complex aliasing artifacts changes sign at the Nyquist frequency. C, A fast Fourier transform (FFT) was applied in the temporal dimension, and the resulting signal was filtered using a Fermi filter to remove the aliasing artifacts. D, The inverse FFT (iFFT) in the temporal dimension resulted in unaliased dynamic images that had nominally twice the temporal resolution

FIGURE S3 Systolic magnitude (gray) and absolute velocity 4D flow images (color) targeting the circle of Willis of subject S6 with different FOV sizes, 1DRF or 2DRF, and UNFOLD as indicated. The nominal acquisition time and nominal temporal resolution Δt are given in the headlines. A, Full FOV data (III) excited 1D selectively, and, B, full FOVL data (I) excited with RFL. C,E, Quarter FOV data (III^{4x}) and, D,F, half FOVL data (I^{2x}) reconstructed without (C,D) and with (E,F) UNFOLD. G, Full FOV data (III) excited 1D selectively and, H, full FOVS data (II) excited with RFS. I,K, Sixth FOV data (III^{6x}) and, J,L, half FOVS data (II^{2x}) reconstructed without (I,J) and with (K,L) UNFOLD. The UNFOLD technique effectively removed the aliasing in data sets (I^{2x}) and (II^{2x}) near the edges of

the reduced FOV (rFOV) (D,J, white arrows), resulting in image quality equivalent to conventionally reconstructed data sets (I) and (II) (B,H), but with doubled the nominal temporal resolution (F,L). Applying UNFOLD to data sets (III^{4x}) and (III^{6x}), however, removed only static first-order aliasing, whereas second-order aliasing remained visible (E,K, white arrow). Furthermore, the static aliasing in scans (I^{2x}) and (II^{2x}) near the edges of the rFOV (D,J, white arrows) indicates where dynamic aliasing may occur when the bandwidth of the data is larger than the UNFOLD Fermi filter. Abbreviations: FOVL = $256 \times 96 \times 96 \text{ mm}^3$, the rFOV adjusted to the FOV of RFL; FOVS = $256 \times 64 \times 64 \text{ mm}^3$, the rFOV adjusted to the FOV of RFS

FIGURE S4 Time-resolved flow curves through the internal carotid arteries of all subjects obtained with the 2DRF data sets (I and II) reconstructed without and with UNFOLD $E_f = 0.8N_y$ and $E_f = 0.5N_y$, and flow curves obtained with the 1DRF data set (III)

FIGURE S5 Bar plots visualizing the SNR in static tissue for 1DRF (first column) and 2DRF RFL (second column) and RFS (third column). The corresponding data sets (III, I, and II) were reconstructed without (blue) and with UNFOLD using $E_f = 0.5N_y$ (red) and $E_f = 0.8N_y$ (yellow). A, The SNR relative to reference data set (III) without UNFOLD reconstruction and, B, the SNR relative to reconstruction without UNFOLD and, C, the SNR relative to 1DRF in percentage. Error bars indicate the corresponding SD over all volunteers

TABLE S1 A, Relative mean difference in peak flow between 1DRF excitation and 2DRF excitations RFL or RFS for the ICA, BA, and lMCA, and rMCA. 2DRF acquisitions were reconstructed without UNFOLD (line 1) or with UNFOLD with $E_f = 0.5 N_y$ (line 2) or $E_f = 0.8 N_y$ (line 3). B, Relative mean difference in peak velocity between 1DRF excitation and 2DRF excitations RFL or RFS for the ICA, BA, lMCA, and rMCA. 2DRF acquisitions were reconstructed without UNFOLD (line 1) or with UNFOLD with $E_f = 0.5 N_y$ (line 2) or $E_f = 0.8 N_y$ (line 3). C, Relative mean difference in peak flow between reconstructions without and with UNFOLD with $E_f = 0.5N_y$ (line 1) or $E_f = 0.8N_y$ (line 2) for 2DRF excitations RFL and RFS and the ICA, BA, lMCA, and rMCA. D, Relative mean difference in blood-flow volume per cardiac cycle between reconstructions without and with UNFOLD with $E_f = 0.5N_y$ (line 1) or $E_f = 0.8N_y$ (line 2) for 2DRF excitations RFL and RFS and the ICA, BA, lMCA, and rMCA. Abbreviations: BA, basilar artery; ICA, internal carotid artery; lMCA, left middle cerebral artery; rMCA, right middle cerebral artery

How to cite this article: Wink C, Bassenge JP, Ferrazzi G, Schaeffter T, Schmitter S. 4D flow imaging with UNFOLD in a reduced FOV.

Magn Reson Med. 2020;84:327–338.

<https://doi.org/10.1002/mrm.28120>